A Noncoherent Massive MIMO System Employing Beamspace Techniques

Stephan Bucher, *Graduate Student Member, IEEE,* George Yammine, *Graduate Student Member, IEEE,* Robert F.H. Fischer, *Senior Member, IEEE,* Christian Waldschmidt, *Senior Member, IEEE*

***Abstract*—Noncoherent detection schemes are an appealing and low-complexity alternative in multi-user massive MIMO uplink systems compared to classical coherent detection algorithms, since no actual channel knowledge is required at the receiver. For noncoherent multi-user detection to function, the induced power at the base station is utilized to separate the different users. However, spatial separation is impossible when the users are located in the far-field of the receiving antenna array. Consequently, noncoherent detection fails in such scenarios. To this end, beamspace techniques can be applied, focusing the energy of the incident wave to a smaller subset of the receive antennas and enabling again the noncoherent detection scheme. This paper analyzes the beamspace capabilities of a dielectric lens and an analog beamforming network applied at the receiver. Furthermore, a sub-array architecture is proposed, relaxing the design requirements for practical implementation. It is shown that noncoherent detection in combination with beamspace techniques performs comparably to channel-estimation-based detection. In addition, the sub-array architecture revealed a significant performance enhancement accompanied by a reduced user separability.**

I. Introduction

MASSIVE multiple-input/multiple-output (MIMO) is one of the most promising key technologies to satisfy the rising demand of high spectral and power efficiency for next generation wireless communication systems [1]–[5]. Evolved from multi-user MIMO, where several users simultaneously communicate with a central base station (BS) equipped with a moderate number of antennas, massive MIMO employs antenna arrays with an order of magnitude more elements. In order to exploit the benefits in terms of enhanced capacity and energy efficiency due to the increased number of BS antennas, accurate channel state information (CSI) has to be available. The main method for CSI acquisition is pilot signaling, where predefined orthogonal pilot signals are transmitted. The process of gathering CSI has been studied extensively [6]–[8]. However, the channel estimation process can quickly become very challenging with the rising number of channels coefficients to be estimated. Furthermore, the accuracy of the CSI can be affected by the re-use of training sequences in other communication cells, widely known as the pilot contamination problem [9], [10].

In order to overcome the issues of channel estimation, an alternative approach in the uplink is proposed in [11], [12], where noncoherent detection methods are applied at the BS to recover the individual transmitted signals of the users. Inspired from ultra-wideband communication systems, no actual channel knowledge is utilized and required, but the per-user received power induced at the antenna array of the BS, i.e., the user-specific power-space profile (PSP). The presented schemes in [11], [12] show results comparable to CSI-based (coherent) detection [13] but reduced complexity for channel estimation and no need for (perfect) synchronization of the local oscillators. This holds as long as the users can be spatially separated at the BS based on their PSPs. Otherwise, noncoherent detection fails when no spatial separation is given, or rather, distinctive PSPs exist. In order to provide favorable PSPs, the BS has to be physically large and the users have to be located in the near-field of the receive array as shown in [14]. A better user separability can be achieved by employing directional antennas at the BS [15].

Basically, for practical implementation purposes, the receive antenna array should be preferably of compact size. However, when shrinking the BS size, and when the users are located in the far-field, no favorable PSPs arise making noncoherent detection impossible. Consequently, it is highly desirable to obtain distinctive PSPs also in the present case. This can be provided by utilizing beamspace techniques, where the energy of the incoming signal is focused on a smaller subset of the receiving antennas. Such techniques can be realized in the analog or in the digital domain using analog beamforming networks [16], [17] or equivalent digital signal processing algorithms [18]–[20], respectively. Furthermore, a dielectric lens in front of the large BS antenna array has also the corresponding focusing properties, which is proposed for coherent hybrid analog/digital massive MIMO transceivers in the uplink in [21]–[24] and for a coherent lens-embedded massive MIMO system in the downlink in [25], [26]. For a proof of concept, a lens approach has been investigated for noncoherent transmission in [27], where very simplified channel and lens models have been utilized.

This work evaluates the lens-embedded system on the basis of a lens model derived from Fourier optics and for a cluster-based channel model. In addition, analog beamforming structures are investigated for noncoherent transmission as well. Furthermore, since the full-array lens or the analog beamformer might reach the limits of a practical implemen-

S. Bucher and C. Waldschmidt are with the Institute of Microwave Engineering, Ulm University, 89081 Ulm, Germany (e-mail: stephan.bucher@uni-ulm.de, christian.waldschmidt@uni-ulm.de)

G. Yammine and R. F.H. Fischer are with the Institute of Communications Engineering, Ulm University, 89081 Ulm, Germany (e-mail: george.yammine@uni-ulm.de, robert.fischer@uni-ulm.de)

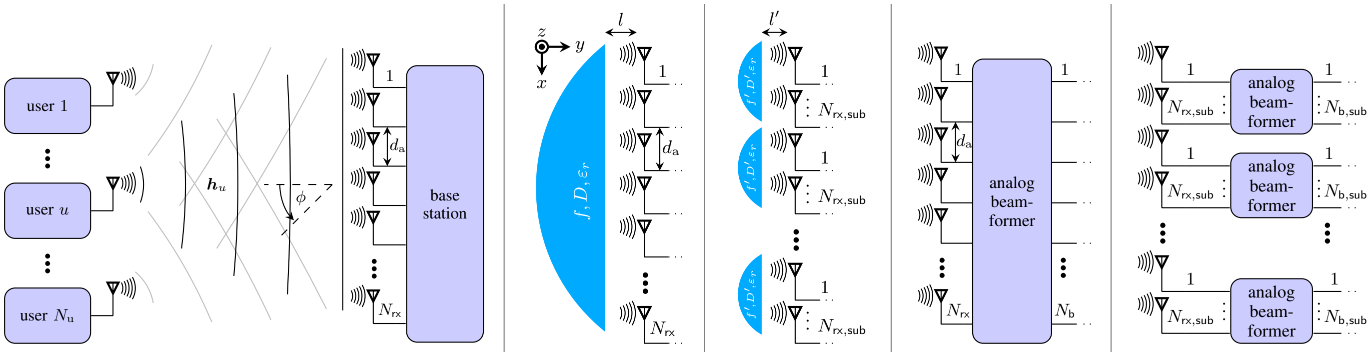

Fig. 1. (a) Conventional massive MIMO uplink system. (b)–(e) Proposed beamspace architecture at the base station for noncoherent detection: (b) full-array lens, (c) sub-array lens, (d) full-array analog beamformer, and (e) sub-array analog beamformer.

tation, a sub-array approach is proposed to relax the design requirements.

Since no distribution network of a high-quality phase reference and no (perfect) synchronization is needed for noncoherent transmission, independent local oscillators at the BS can be employed reducing the complexity of the distribution network. However, the phase progression between adjacent receive channels is lost after downconversion to baseband. Hence, digital beamforming cannot be applied in the given setup and is not examined in this paper.

In summary, the noncoherent detection approach fails when users are located in the far-field. The contribution of this work is to unite the individual common known concepts of beamspace techniques, sub-array architecture, and noncoherent detection and analyze these approaches jointly. To this purpose, sophisticated and physically accurate beamspace technique and channel models are utilized, which guarantee an evaluation under realistic conditions.

This paper is organized as follows. Section II introduces the system model containing an overview of the proposed massive MIMO system with beamspace techniques for noncoherent detection. Furthermore, the respective models for the dielectric lens and the analog beamformer are derived. Section III details the cluster-based channel model and the integration of the corresponding beamspace models. The noncoherent detection algorithm is reviewed in Section III. Numerical results for full- and sub-array architectures are shown in Section IV. Finally, conclusions are drawn in Section V.

Notations: In this paper, bold-faced capital letters and bold-faced small letters denote matrices and column vectors, respectively. Superscripts $(\cdot)^{\mathsf{T}}$ and $(\cdot)^{\mathsf{H}}$ indicate matrix transpose and matrix conjugate transpose, respectively. The operators $\circ$, $\otimes$, $\mathrm{E}\{\cdot\}$, $\mathscr{F}\{\cdot\}$ and $\mathrm{DFT}\{\cdot\}$ denote the entry-wise product of two vectors (or matrices), the Kronecker product, the expectation, the Fourier transform, and the discrete Fourier transform, respectively. $\boldsymbol{I}_N$ is the $N \times N$ identity matrix and $||\cdot||_{\mathrm{F}}$ is the Frobenius norm of a matrix.

II. System Model

A. System Overview

In this paper, a multi-user uplink system is considered, where N_{u} single-antenna user transmit to a central base station. At the base station a uniform linear array with a very large number of receive antennas $N_{\mathsf{rx}} \gg N_{\mathsf{u}}$ and an inter-element distance of d_{a} is employed. The users simultaneously transmit independent data streams to the receiver and noncoherent detection methods are applied at the base station to recover the data. The conventional massive MIMO system is depicted in Fig. 1a. In order to ensure the required spatial separation of each individual user at the base station for the noncoherent detection scheme, beamspace techniques are utilized focusing the energy on a smaller subset of the receiving array. These techniques are described in the following.

1) Beamspace System Architectures: Energy focusing at the base station can be provided either by a dielectric lens embedded at the receiver of the conventional system (attached in front of the antenna elements) as depicted in Fig. 1b or by a beamforming structure in the analog domain (after the antennas but before the downconversion and the analog-to-digital conversion) as illustrated in Fig. 1d.

The dielectric lens acts as a phase shifter producing a converging wavefront from a plane wave input and concentrates the power of the incident wave in the focal plane depending on the angle of arrival of the wave. The relevant design parameters of the lens are the focal length f, the lens aperture D, the electric permitivity of the lens material ε_r, as well as the distance l between the lens and the receiving antenna array (generally equal to the focal length).

In case of the analog beamformer, the input signals are superimposed constructively using a phase-shifting network or time-delay-based network, where in both cases the output ports (beam ports) N_{b} remain the same as the number of input ports (N_{rx}). Thus, the energy is focused to one of the beam ports depending on the direction of the incoming signal. For instance, the phase-shifting network can be realized by discrete phase shifters together with power dividers and combiners using a Butler matrix [17], [28]. A time-delay-based network, for example, can be implemented by a Rotman lens [16], [29], [30], which artificially introduces time delays to focus the incoming wave. In general, both the Butler matrix and the Rotman lens require an antenna number, which is a power of two, i.e., $N_{\mathsf{rx}} = 2^N$, $N \in \mathbb{N}$.

In Fig. 1b and Fig. 1d the lens aperture covers the entire receiving array and the input signals of the analog beamformer

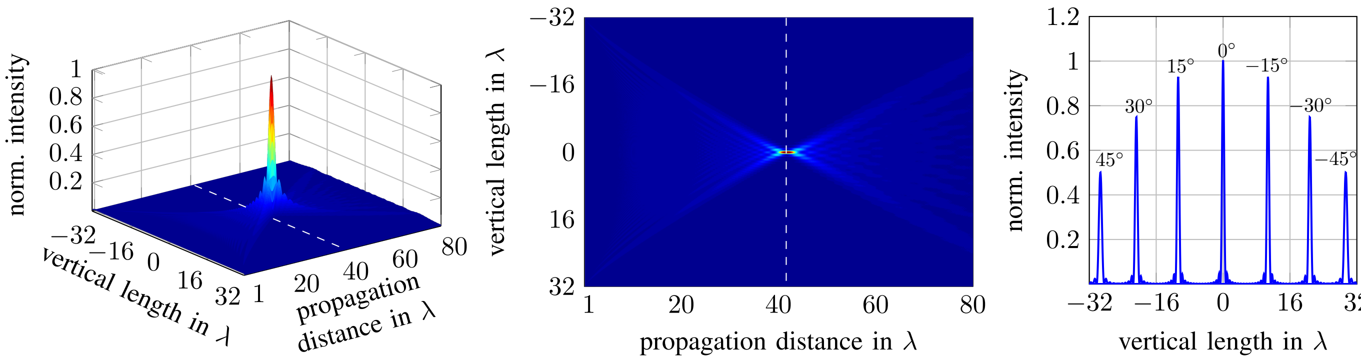

(a) (b) (c)

Fig. 2. Propagation characteristics of a dielectric lens with $D=64\lambda$ and $f=41.6\lambda$. (a) 3D- and (b) 2D-field distribution of an incident wave at $\phi=0°$. The dashed white line represents the focal plane at distance f. (c) Cross section intensity at the focal length f for several angle of arrivals ϕ (normalized to the maximum intensity at $\phi=0°$).

are processed jointly. This full-array architecture provides optimal results in view of its energy-focusing capabilities. However, the practical implementation of both architectures can be extremely challenging as the size of the lens is very large at low carrier frequencies and the complexity of the analog beamformer scales with the number of receive antennas. Consequently, a more practical approach is to resort to a sub-array architecture, where the full-array is divided into several sub-arrays as depicted in Fig. 1c and Fig. 1e. It is assumed that the receiving array is splitted into N_{sub} equal-size sub-arrays, where each sub-array has $N_{\mathsf{rx,sub}}=N_{\mathsf{b,sub}}=N_{\mathsf{rx}}/N_{\mathsf{sub}}$ antennas or beam ports. In case of the lens architecture, each sub-array is equipped with a small-size lens, which aperture is downsized by the number of sub-arrays according to $D'=D/N_{\mathsf{sub}}$.

In order to evaluate the performance of the proposed beamspace architectures, appropriate models for the lens and the analog beamforming have been developed, which are described in the following.

2) Dielectric Lens Model: The lens aperture is assumed to lie in the x-z-plane and is illuminated in positive y-direction. Applying the Huygens–Fresnel principle for parallel planes and the Fresnel approximation, the field distribution $U_y(x,z)$ at a distance y behind the lens can be expressed as [31]

$$U_y(x,z) = \mathscr{F}^{-1}\left\{\mathscr{F}\left\{U_0(x,z)\right\}\cdot\mathscr{F}\left\{\tilde{h}_y(x,z)\right\}\right\}\,, \quad (1)$$

where $U_0(x,z)$ is the field distribution at the aperture. The term $\tilde{h}_y(x,z)$ in (1) is the impulse response of the free-space propagation given by [31]

$$\tilde{h}_y(x,z) = \frac{\mathrm{e}^{\mathrm{j}ky}}{\mathrm{j}\lambda y}\,\mathrm{e}^{\mathrm{j}k\frac{x^2+z^2}{2y}}\,, \quad (2)$$

where $k=2\pi/\lambda$ is the wavenumber, λ is the wavelength, and $\mathrm{j}=\sqrt{-1}$. Physically speaking, the field distribution at distance y is given by the inverse Fourier transform ($\mathscr{F}^{-1}\{\cdot\}$) of the product of the Fourier-transformed initial field right at the aperture and of a Fourier-transformed quadratic phase exponential and a multiplicative factor.

Since the array configuration at the base station is considered as a one-dimensional uniform linear array, the dimensionality of the lens model can be reduced in the same manner. In the following, the base station antennas are positioned along the x-axis and, therefore, only the field distribution along the x-axis of the lens is relevant. Thus (1) changes accordingly to

$$U_y(x) = \mathscr{F}^{-1}\left\{\mathscr{F}\left\{U_0(x)\right\}\cdot\mathscr{F}\left\{\tilde{h}_y(x)\right\}\right\}\,. \quad (3)$$

For computation purposes, the field distribution in x-direction is sampled within the range of an observation window of size X using a sampling distance of Δx. The total number of samples is $N_{\mathsf{s}}=X/\Delta x$. The field in y-direction is calculated using discrete steps of Δy. The complex field vector $\boldsymbol{u}_{n\Delta y}$ at a distance $n\Delta y$ is then given as

$$\boldsymbol{u}_{n\Delta y} = \begin{bmatrix} u_{n\Delta y}\left[-N_{\mathsf{s}}/2+1\right] \\ \vdots \\ u_{n\Delta y}\left[m'\right] \\ \vdots \\ u_{n\Delta y}\left[N_{\mathsf{s}}/2\right] \end{bmatrix}\,, \quad (4)$$

where $u_{n\Delta y}\left[m'\right] \overset{\text{def}}{=} U_{y=n\Delta y}(m'\Delta x)$. The field vector $\boldsymbol{u}_{n\Delta y}$ is obtained recursively from the field $\boldsymbol{u}_{(n-1)\Delta y}$ of the previous sampling step as in [26] according to

$$\boldsymbol{u}_{n\Delta y} = \mathrm{DFT}^{-1}\left\{\mathrm{DFT}\left\{\boldsymbol{u}_{(n-1)\Delta y}\right\}\circ\mathrm{DFT}\left\{\tilde{\boldsymbol{h}}_{\Delta y}\right\}\right\}\,, \quad (5)$$

where

$$\tilde{\boldsymbol{h}}_{\Delta y} = \begin{bmatrix} \tilde{h}_{\Delta y}\left[-N_{\mathsf{s}}/2+1\right] \\ \vdots \\ \tilde{h}_{\Delta y}\left[m'\right] \\ \vdots \\ \tilde{h}_{\Delta y}\left[N_{\mathsf{s}}/2\right] \end{bmatrix}\,, \quad (6)$$

and

$$\tilde{h}_{\Delta y}\left[m'\right] = \frac{\mathrm{e}^{\mathrm{j}k\Delta y}}{\mathrm{j}\lambda\Delta y}\,\mathrm{e}^{\mathrm{j}k\frac{(m'\Delta x)^2}{2\Delta y}}\,. \quad (7)$$

Applying a thin lens assumption, the initial field distribution $\boldsymbol{u}_0$ at the surface of the lens is given by [26], [31]

$$u_0\left[m'\right] = P\left[m'\right]\mathrm{e}^{-\mathrm{j}k\left(\frac{(m'\Delta x)^2}{2f}+m'\Delta x\sin(\phi)\right)}\,, \quad (8)$$

where f is known as the focal length, ϕ is the angle of the incident plane wave, and $P\left[m'\right]$ is the pupil function. The pupil function takes into account the aperture of the lens, i.e., the opening available to collect electromagnetic energy. As the amount of collected energy depends on the angle of the incident wave, the pupil function is

$$P[m'] = \begin{cases} 1, & |m'\Delta x| \leq \frac{1}{2} D \cos(\phi) \\ 0, & \text{otherwise} \end{cases} . \tag{9}$$

The propagation and focusing characteristics of the dielectric lens is exemplarily illustrated for $D = 64\lambda$ and $f = 41.6\lambda$ in Fig. 2. When a plane wave impinges on the lens, the power is concentrated at the focal distance (hotspot) and follows a sinc function (see Fig. 2). The location of the hotspot varies along the focal plane with respect to the angle of arrival of the incident wave. Furthermore, the width of the footprint increases for larger $|\phi|$, while the power peak decreases (see Fig. 2c). The ratio of focal length to aperture diameter (f/D) of the lens determines the scanning angle range and the resolution of spatial angle. Increasing f/D leads to a larger distance of two adjacent focal spots for the same angle of arrival. Consequently, the resolution is improved. However, the larger f/D, the smaller the scanning angle range leading to a tradeoff between resolution and coverage angle. These observations are consistent with that reported in prior works based on experiments [32], [33]. For the given configuration, $f/D = 0.65$ and the scanning range amounts to approximately $\pm 45°$.

Since the receive array is placed behind the dielectric lens at the focal distance, the array response as function of the incident angle can be obtained from the field distribution sampled at the position of the N_{rx} antenna elements, which are uniformly spaced by the antenna distance d_{a}. Thus, the array response can be expressed as

$$\boldsymbol{a}^{\mathsf{lens,full}}(\phi) = \begin{bmatrix} u_f[d[1]] \\ u_f[d[2]] \\ \vdots \\ u_f[d[N_{\mathsf{rx}}]] \end{bmatrix}, \tag{10}$$

where $u_f[m']$ denotes the field distribution at the focal length f and $d[m] = \frac{d_{\mathrm{a}}}{\Delta x}(m - N_{\mathsf{rx}}/2)$ represents the position of the mth base station antenna along the x-axis.

In case of the sub-array architecture, the field distribution of the lens is computed for a small-sized lens of $D' = D/N_{\mathsf{sub}}$. The focal length is downsized in the same manner to $f' = f/N_{\mathsf{sub}}$ such that the ratio f'/D' is kept constant in order to provide the same scanning range. Accordingly, the array response for the sub-array is then

$$\boldsymbol{a}^{\mathsf{lens,sub}}(\phi) = \begin{bmatrix} u_{f'}[d[1]] \\ u_{f'}[d[2]] \\ \vdots \\ u_{f'}[d[N_{\mathsf{rx,sub}}]] \end{bmatrix}, \tag{11}$$

where $u_{f'}[m']$ denotes the field intensity at the focal length f' and $d[m_{\mathsf{sub}}] = \frac{d_{\mathrm{a}}}{\Delta x}(m_{\mathsf{sub}} - N_{\mathsf{rx,sub}}/2)$ indicates the corresponding position of the m_{sub}th antenna of the sub-array.

3) Analog Beamforming Model: In general, the analog beamforming network processes the incoming signal from N_{rx} antennas in order to form N_{b} beams corresponding to N_{b} pre-configured angles of arrival. Hence, a wavefront arriving with a proper phase front at the array is focused at the corresponding beam port. In other words, signals are superimposed to add coherently at the beam port for a defined direction. Without loss of generality, it is assumed that $N_{\mathsf{rx}} = N_{\mathsf{b}}$. Considering the full-array architecture, the multiport network can be described by an $N_{\mathsf{b}} \times N_{\mathsf{rx}}$ matrix [30]

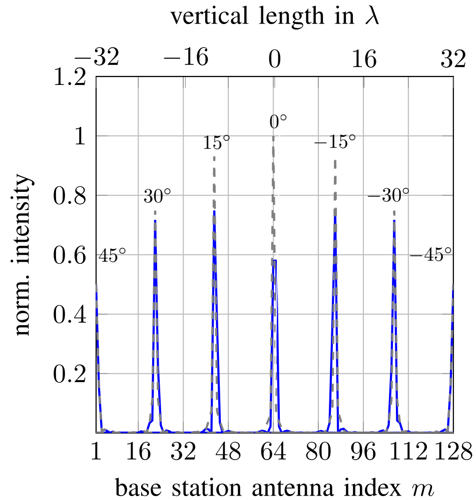

Fig. 3. Field intensity (——) for several angle of arrivals ϕ of the incoming plane wave at the output of a full-array analog beamformer. The scanning angle range is $\pm 45°$, $N_{\mathsf{rx}} = N_{\mathsf{b}} = 128$, and $d_{\mathrm{a}} = \lambda/2$. The dashed gray plot (– – –) represents the field intensity when the angle of arrival ϕ is perfectly matched to the next available angle bin.

$$\boldsymbol{A}^{\mathsf{ABF,full}} = [\tilde{\boldsymbol{a}}_{N_{\mathsf{rx}}}(\phi_1^{\mathsf{full}}), \tilde{\boldsymbol{a}}_{N_{\mathsf{rx}}}(\phi_2^{\mathsf{full}}), \ldots, \tilde{\boldsymbol{a}}_{N_{\mathsf{rx}}}(\phi_{N_{\mathsf{b}}}^{\mathsf{full}})]^{\mathsf{H}}, \tag{12}$$

where $\tilde{\boldsymbol{a}}_{N_{\mathsf{rx}}}(\phi)$ is the steering vector $\boldsymbol{a}_{N_{\mathsf{rx}}}(\phi)$ of a uniform linear array with N_{rx} elements weighted by the aperture loss depending on the angle of arrival ϕ, i.e.,

$$\tilde{\boldsymbol{a}}_{N_{\mathsf{rx}}}(\phi) = \cos(\phi)\, \boldsymbol{a}_{N_{\mathsf{rx}}}(\phi) = \frac{\cos(\phi)}{\sqrt{N_{\mathsf{rx}}}} \begin{bmatrix} 1 \\ \mathrm{e}^{-\mathrm{j}kd_{\mathrm{a}}\sin(\phi)} \\ \vdots \\ \mathrm{e}^{-\mathrm{j}k(N_{\mathsf{rx}}-1)d_{\mathrm{a}}\sin(\phi)} \end{bmatrix}, \tag{13}$$

and the set $\{\phi_1^{\mathsf{full}}, \phi_2^{\mathsf{full}}, \cdots, \phi_{N_{\mathsf{b}}}^{\mathsf{full}}\}$ in represents the sweeping angles of the beam ports.

In the same manner, the sub-array architecture can be characterized by an $N_{\mathsf{b}} \times N_{\mathsf{rx}}$ block diagonal matrix

$$\boldsymbol{A}^{\mathsf{ABF,sub}} = \boldsymbol{I}_{N_{\mathsf{sub}}} \otimes [\tilde{\boldsymbol{a}}_{N_{\mathsf{rx,sub}}}(\phi_1^{\mathsf{sub}}), \ldots, \tilde{\boldsymbol{a}}_{N_{\mathsf{rx,sub}}}(\phi_{N_{\mathsf{b,sub}}}^{\mathsf{sub}})]^{\mathsf{H}}, \tag{14}$$

where $\tilde{\boldsymbol{a}}_{N_{\mathsf{rx,sub}}}(\phi)$ is the weighted steering vector of the sub-array with $N_{\mathsf{rx,sub}}$ elements (compare (13)) and $\{\phi_1^{\mathsf{sub}}, \cdots, \phi_{N_{\mathsf{b,sub}}}^{\mathsf{sub}}\}$ is the corresponding set of sweeping angles for the $N_{\mathsf{b,sub}}$ beam ports.

The set of sweeping angles for both the full-array and the sub-array architecture are evenly distributed within the desired scanning range of the receiver. In other words, the angular domain is sampled with fixed angular bins, whereby the number of bins and the angular resolution is determined by the number of beam ports, or rather, the number of receive antennas. Consequently, the sub-array architecture exhibits a lower resolution and a smaller number of angular bins in comparison to a full-array architecture maintaining the same scanning range.

The analog beamforming approach differs from the lens-embedded system especially by the fact, that the energy of the incoming wave is focused to one of the beam ports and there is a discrete field distribution (quantized by the number of beam ports or antenna ports, respectively). Conversely, regarding the lens approach, the energy is focused in the focal plane and the continuous field is then sampled by the respective antenna positions.

An example for the energy focusing capabilities of the full-array analog beamforming structure is depicted in Fig. 3 for several angle of arrivals ϕ of an incident plane wave using (12). The number of antennas and beam ports are $N_{\mathsf{rx}} = N_{\mathsf{b}} = 128$ and the antenna distance is $d_{\mathrm{a}} = \lambda/2$. The set of sweeping angles is equally distributed in a scanning angle range of $\pm 45°$. It can be observed that when the angle of arrival does not perfectly match any available angle bin of the beamformer (or rather does not coincide with the preconfigured angle of arrival each beam/antenna port is assigned to), the peak intensity is reduced. The same applies for larger $|\phi|$ caused by the aperture loss.

B. Channel Model

First, the propagation channel without any beamspace techniques is considered. As previously mentioned, a massive MIMO channel with a uniform linear array of N_{rx} antennas at the base station and a single antenna at each user are studied. Here, a geometry-based stochastic channel model, namely the COST 2100 channel model [34], [35], is used and adapted appropriately. This channel model emulates physical scattering objects by placing clusters randomly in the topological simulation area. Each cluster consists of groups of multi-path components (MPC), which the parameters thereof such as direction and complex amplitude are calculated from the geometry of the simulation region. Basically, a distinction is made between four kinds of clusters. These are local clusters (scatterers surrounding the users and the BS), single clusters (scattering with one object), twin clusters (scattering with multiple objects), and common clusters (user and BS share the same set of clusters). Furthermore, line-of-sight propagation between the user and the BS can be taken into account as well. However, reducing the complexity, in the following only local clusters are considered, which are uniformly distributed around the users in the horizontal/azimuthal plane and are characterized by a spatial spread. Furthermore, plane waves impinging at the base station are assumed. When no beamspace techniques are applied, the complex channel vector $\boldsymbol{h}_u$ for the uth user can be described as

$$\boldsymbol{h}_u = \sum_{p=1}^{N_{u,p}} a_{u,p}^{\mathsf{MPC}} \, \boldsymbol{a}_{N_{\mathsf{rx}}}(\phi_{u,p}^{\mathsf{MPC}}) \, , \tag{15}$$

where $a_{u,p}^{\mathsf{MPC}}$ denotes the complex amplitude of the pth multi-path component originating from the local clusters of the uth user, $\phi_{u,p}^{\mathsf{MPC}}$ is the corresponding angle of arrival, and $N_{u,p}$ is the total number of multi-path components of the uth user. $\boldsymbol{a}_{N_{\mathsf{rx}}}(\phi_{u,p}^{\mathsf{MPC}})$ represents the steering vector of the uniform linear array already introduced in (13).

1) Dielectric Lens: In order to integrate the dielectric lens in the present channel model, the steering vector of the uniform linear array is replaced by the array response vector of the already introduced lens model. Considering the full-array architecture, the complex channel vector of the uth user can be expressed as

$$\boldsymbol{h}_u^{\mathsf{lens,full}} = \sum_{p=1}^{N_{u,p}} a_{u,p}^{\mathsf{MPC}} \, \boldsymbol{a}^{\mathsf{lens,full}}(\phi_{u,p}^{\mathsf{MPC}}) \, . \tag{16}$$

The same procedure is done in case of the sub-array architecture. However, as a plane wave assumption is applied, the change in phase of the multi-path components among the sub-arrays is taken into account. The sub-channel vector $\boldsymbol{h}_{u,n}^{\mathsf{lens,sub}}$ of the nth sub-array and the uth user is then given as

$$\boldsymbol{h}_{u,n}^{\mathsf{lens,sub}} = \sum_{p=1}^{N_{u,p}} a_{u,p}^{\mathsf{MPC}} \, \boldsymbol{a}^{\mathsf{lens,sub}}(\phi_{u,p}^{\mathsf{MPC}}) \, \mathrm{e}^{-\mathrm{j}k(n-1)d_{\mathsf{sub}} \sin\left(\phi_{u,p}^{\mathsf{MPC}}\right)} \, , \tag{17}$$

where $d_{\mathsf{sub}} = N_{\mathsf{rx,sub}} \, d_{\mathrm{a}}$ denotes the distance between adjacent sub-arrays. Stacking of $\boldsymbol{h}_{u,n}^{\mathsf{lens,sub}}$ of the individual sub-arrays yields the entire channel coefficient column vector of the uth user according to

$$\boldsymbol{h}_u^{\mathsf{lens,sub}} = \begin{bmatrix} \boldsymbol{h}_{u,1}^{\mathsf{lens,sub}} \\ \boldsymbol{h}_{u,2}^{\mathsf{lens,sub}} \\ \vdots \\ \boldsymbol{h}_{u,N_{\mathsf{sub}}}^{\mathsf{lens,sub}} \end{bmatrix} . \tag{18}$$

2) Analog Beamforming: Given the analog beamforming model as previously stated, the extended channel column vector is simply the product of the beamforming matrix and the channel vector of the uth user of the conventional system. For the full-array architecture it reads

$$\boldsymbol{h}_u^{\mathsf{ABF,full}} = \boldsymbol{A}^{\mathsf{ABF,full}} \boldsymbol{h}_u \, . \tag{19}$$

In the same way, the modified channel vector using the sub-array approach is as follows:

$$\boldsymbol{h}_u^{\mathsf{ABF,sub}} = \boldsymbol{A}^{\mathsf{ABF,sub}} \boldsymbol{h}_u \, . \tag{20}$$

III. Noncoherent Detection

Considering the massive MIMO uplink system as depicted in Fig. 1a, the noncoherent detection of each user is performed block-wise over a temporal block. Assuming the channel to be constant over a transmission burst, the received signal block $\boldsymbol{R}$ of N_{rx} receive antennas and over N_{bl} time steps can be written as

$$\boldsymbol{R} = \sum_{u=1}^{N_{\mathsf{u}}} \boldsymbol{h}_u \boldsymbol{b}_u^{\mathsf{T}} + \boldsymbol{N} = \boldsymbol{H}\boldsymbol{B} + \boldsymbol{N} \, , \tag{21}$$

where $\boldsymbol{h}_u = [h_{1,u}, \ldots, h_{N_{\mathsf{rx}},u}]^{\mathsf{T}}$ collects the complex-valued channel coefficients of the uth user (equal to the corresponding channel coefficient vector $\boldsymbol{h}_u^{\mathsf{lens}}$ or $\boldsymbol{h}_u^{\mathsf{ABF}}$ when beamspace techniques are applied), $\boldsymbol{b}_u^{\mathsf{T}} = [b_{0,u}, b_{1,u}, \ldots, b_{N_{\mathsf{bl}}-1,u}]$ consists of the transmit symbols $b_{k,u}$ of each user u at time step k, and $\boldsymbol{N}$ gathers the zero-mean circular-symmetric complex Gaussian noise samples $n_{m,k}$ with variance σ_n^2 at the mth receive antenna at time step k. As in [30], it is assumed that the noise is still Gaussian distributed even if the introduced beamspace techniques are applied. Alternatively, the receive block $\boldsymbol{R}$ in (21) can be represented by the channel matrix $\boldsymbol{H} = [\boldsymbol{h}_1, \ldots, \boldsymbol{h}_{N_\mathsf{u}}]$ (equal to the corresponding channel matrix $\boldsymbol{H}^\mathsf{lens} = [\boldsymbol{h}_1^\mathsf{lens}, \ldots, \boldsymbol{h}_{N_\mathsf{u}}^\mathsf{lens}]$ or $\boldsymbol{H}^\mathsf{ABF} = [\boldsymbol{h}_1^\mathsf{ABF}, \ldots, \boldsymbol{h}_{N_\mathsf{u}}^\mathsf{ABF}]$ when beamspace techniques are applied) and the transmit symbol matrix $\boldsymbol{B} = [\boldsymbol{b}_1, \ldots, \boldsymbol{b}_{N_\mathsf{u}}]^\mathsf{T}$.

The transmit symbols are differentially encoded unit-magnitude phase-shift keying (DPSK) symbols. To this end, the information symbols $a_{k,u}$ of each user to be transmitted are drawn from an M-ary PSK constellation $\mathcal{M} = \{\mathrm{e}^{\mathrm{j}2\pi i/M} \mid i = 0, 1, \ldots, M-1\}$ and are differentially encoded such that

$$b_{k,u} = a_{k,u}\, b_{k-1,u} \,, \qquad b_{0,u} = 1 \,. \tag{22}$$

The signal-to-noise ratio (SNR) is defined as the ratio of the transmitted energy per PSK symbols $E_\mathsf{s,tx}$ and the noise power spectral density N_0. Due to the use of PSK signals $E_\mathsf{s,tx}/N_0 = 1/\sigma_\mathsf{n}^2$.

The noncoherent detection scheme is based on the $N_\mathsf{bl} \times N_\mathsf{bl}$ correlation matrix

$$\boldsymbol{Z}_u \overset{\text{def}}{=} \boldsymbol{R}^\mathsf{H} \boldsymbol{W}_u \boldsymbol{R} \,, \tag{23}$$

where $\boldsymbol{W}_u \overset{\text{def}}{=} \mathbf{diag}(w_{1,u}, \ldots, w_{N_\mathsf{rx},u})$ is a user-specific diagonal weighting matrix acting as a spatial filter. Knowing the average power induced by each user at the base station (power-space profile, PSP), the weighting coefficients can be optimized to maximize the signal-to-noise-plus-interference ratio (SINR) [12], [36]. Other approaches are matched weighting or antenna windowing [11]. The power-space profile $\boldsymbol{p}_u$ of user u over the receive antennas results from averaging the squared magnitude of the uth channel coefficient vector $\boldsymbol{h}_u$ (or $\boldsymbol{h}_u^\mathsf{lens}$ or $\boldsymbol{h}_u^\mathsf{ABF}$ when beamspace techniques are applied) over different channel realizations, i.e.,

$$\boldsymbol{p}_u \overset{\text{def}}{=} \mathrm{E}\{|\boldsymbol{h}_u|^2\} \,. \tag{24}$$

Using (23), the detection can be done for each user individually (in parallel) by employing decision-feedback differential detection (DFDD) [11]. In this case, decisions are generated successively and previous detected symbols are taken into account. A performance improvement can be achieved by combining DFDD with noncoherent decision-feedback equalization (DFDD/nDFE) [12], where average interference cancellation based on already detected symbols of the other users is performed in addition.

IV. Numerical Results

The symbol error rate performance of the noncoherent detection scheme is evaluated for the conventional massive MIMO uplink system and for the proposed beamspace architectures using DFDD/nDFE. In order to provide a basis for performance comparison, a coherent detection scheme, namely Bell Laboratories layered space-time (BLAST) [37], is evaluated assuming perfect channel knowledge at the receiver. To this end, simulations are carried out for $N_\mathsf{u} = 3$ users and

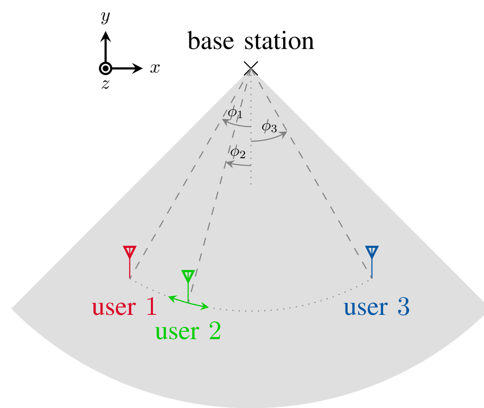

Fig. 4. User and base station arrangement to evaluate the noncoherent massive MIMO system with beamspace techniques. The shaded area ( ) denotes the scanning angle range of the base station.

TABLE I
System configuration and parameterization of propagation channel and noncoherent detection.

System configuration	
number of users N_u	3
number of BS antennas N_rx	128
BS antenna spacing d_a	$\lambda/2$
scanning angle range of BS	$\pm 45°$
user and BS antenna type	omni-directional
angle ϕ_u of user	$\phi_1 = -30°$, ϕ_2, $\phi_3 = 30°$
Propagation channel	
cluster types	local
number of multi-path components $N_{u,p}$	3
angular spread at BS	$\sigma_\mathsf{s} = 8°$
number of different channel realizations per user 2 angle ϕ_2	300,000
channel normalization (power control)	$\|\|\boldsymbol{H}\|\|_\mathrm{F}^2 = N_\mathsf{u}$ $(= \|\|\boldsymbol{H}^\mathsf{lens}\|\|_\mathrm{F}^2 = \|\|\boldsymbol{H}^\mathsf{ABF}\|\|_\mathrm{F}^2)$
Noncoherent detection	
modulation alphabet	4-ary DPSK
block length N_bl	200

a base station employing $N_\mathsf{rx} = 128$ omni-directional antennas arranged as uniform linear array. The inter-element distance amounts to $d_\mathrm{a} = \lambda/2$. The scanning angle range of the base station is assumed to be $\pm 45°$. This configuration corresponds to the situation that the coverage of the BS is equally sectorized into four sectors of $90°$ each. The users equipped with a single omni-directional antenna are placed in front of the BS in such a way that they are located in the far-field and are seen under a given angle ϕ_u as depicted in Fig. 4. The angles of users 1 and 3 are fixed in the following and set to $\phi_1 = -30°$ and $\phi_3 = 30°$, respectively.

Regarding the propagation channel, multi-path propagation is assumed originating from local clusters surrounding the users. The local clusters are uniformly distributed in the horizontal/azimuthal plane and the plane waves impinging at

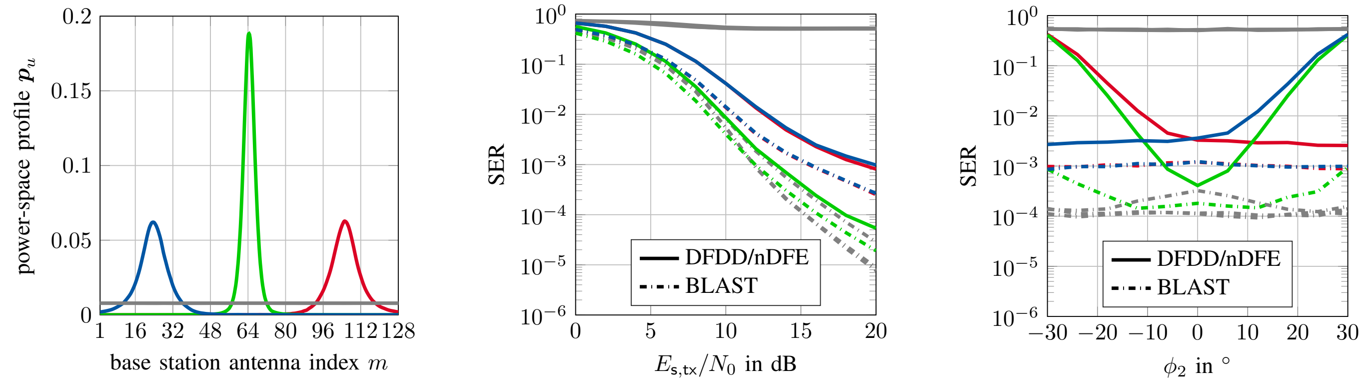

(a) Power-space profile $\boldsymbol{p}_u$ when user 2 at boresight ($\phi_2 = 0°$).

(b) Symbol error rate vs. signal-to-noise ratio when user 2 at boresight ($\phi_2 = 0°$).

(c) Symbol error rate vs. angle ϕ_2 of user 2 for $E_{s,tx}/N_0 \mathrel{\widehat{=}} 15\,\text{dB}$.

Fig. 5. Full-array lens architecture: Power-space profile and symbol error rate performance. Colors correspond to users: user 1 (—/-·-·), user 2 (—/-·-·), user 3 (—/-·-·). Gray plots (—/-·-·) represent results for conventional system without beamspace techniques for each user.

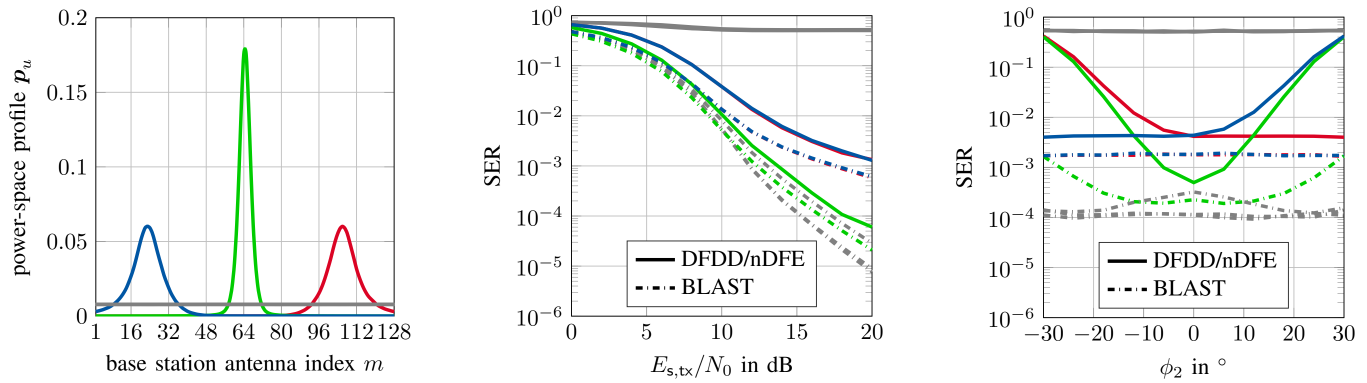

(a) Power-space profile $\boldsymbol{p}_u$ when user 2 at boresight ($\phi_2 = 0°$).

(b) Symbol error rate vs. signal-to-noise ratio when user 2 at boresight ($\phi_2 = 0°$).

(c) Symbol error rate vs. angle ϕ_2 of user 2 for $E_{s,tx}/N_0 \mathrel{\widehat{=}} 15\,\text{dB}$.

Fig. 6. Full-array analog beamforming architecture: Power-space profile and symbol error rate performance. Colors correspond to users: user 1 (—/-·-·), user 2 (—/-·-·), user 3 (—/-·-·). Gray plots (—/-·-·) represent results for conventional system without beamspace techniques for each user.

the BS have an angular spread with standard deviation $\sigma_s = 8°$, which is a reasonable value for urban environments [38]. The number of multi-path components per user is $N_{u,p} = 3$. Since the SER performance is averaged over a different number of channel realizations, 300,000 different channel matrices are acquired from the cluster-based channel model. A power control is utilized assuming that the transmit power of each user is adjusted in such a way that the total sum power induced by all users is the same at the BS. In other words, the respective channel matrices $\boldsymbol{H}$, $\boldsymbol{H}^{\text{lens}}$, and $\boldsymbol{H}^{\text{ABF}}$ are normalized in such a way that $||\boldsymbol{H}||_\text{F}^2 = ||\boldsymbol{H}^{\text{lens}}||_\text{F}^2 = ||\boldsymbol{H}^{\text{ABF}}||_\text{F}^2 = N_u$ providing a fair comparison.

For the noncoherent detection, a block length of $N_{bl} = 200$ is considered, whereby the users transmit quaternary DPSK symbols. A summary of the system configuration as well as of the relevant parameterization of the propagation channel and of the noncoherent detection is given in Table I.

A. Full-Array Architecture

First the full-array architecture is investigated starting with the lens-embedded system. Providing the previously specified scanning angle range of ±45°, the ratio of the aperture size and the focal length of the lens is chosen as $f/D = 0.65$. As the aperture size is predefined by the physical size of the antenna array, i.e., $D = 64\lambda$, the focal length is consequently $f = 41.6\lambda$. Applying the lens-embedded system, the receive power of each user is focused onto a small part of the entire receiving antenna array. Fig. 5a shows the corresponding power-space profile when user 2 is located at boresight ($\phi_2 = 0°$). In the present scenario, the PSP of user 2 exhibits a narrow peak, whereas the induced power of the users 1 and 3 is distributed over a larger range of antennas. Furthermore, the total power of the users 1 and 3 is less. The reduction in power is due to the aperture loss, which is proportional to the angle ϕ_u and which at the same time leads to a broadening of the profiles. Noteworthy, comparing the intensity of the lens in Fig. 2c, the power distribution in the present case is broadened. This is due to the reason that several plane waves having a spatial spread impinge at the base station. On the contrary, the power of each user is equally and uniformly distributed among the receiving antennas when no lens is present.

Fig. 5b shows the symbol error rate vs. the SNR when user 2 is again at boresight. Considering the conventional system,

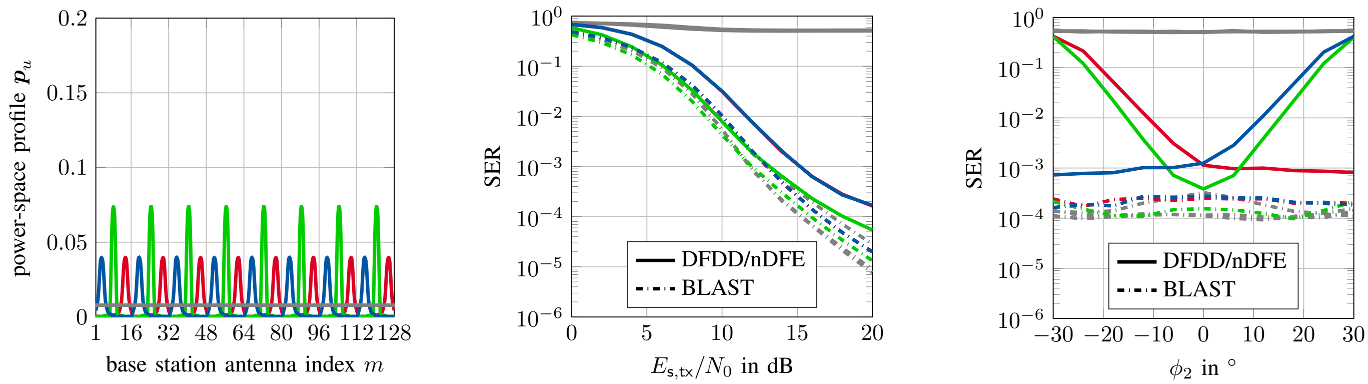

(a) Power-space profile $\boldsymbol{p}_u$ when user 2 at boresight ($\phi_2 = 0°$).

(b) Symbol error rate vs. signal-to-noise ratio when user 2 at boresight ($\phi_2 = 0°$).

(c) Symbol error rate vs. angle ϕ_2 of user 2 for $E_{\mathsf{s,tx}}/N_0 \,\hat{=}\, 15\,\text{dB}$.

Fig. 7. Sub-array lens architecture: Power-space profile and symbol error rate performance. Colors correspond to users: user 1 (—/-·-), user 2 (—/-·-), user 3 (—/-·-). Gray plots (—/-·-) represent results for conventional system without beamspace techniques for each user.

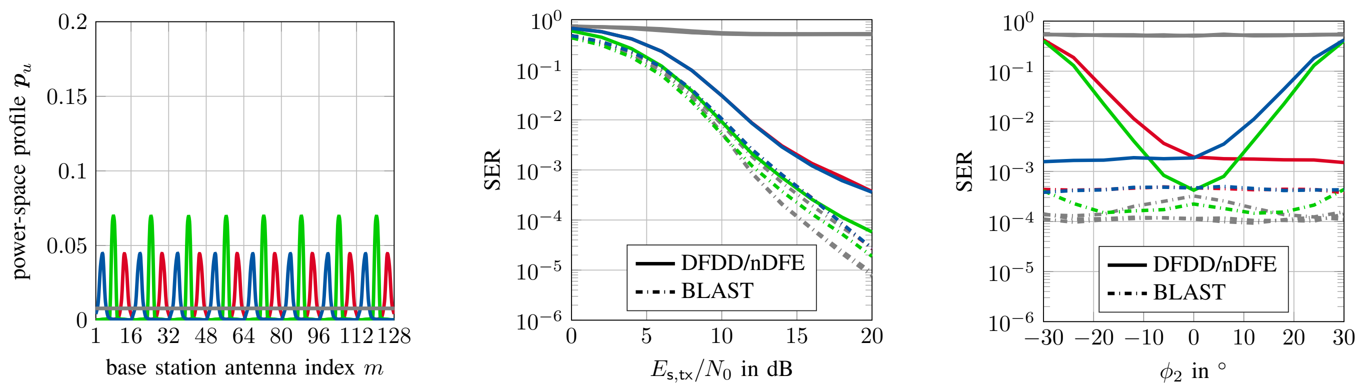

(a) Power-space profile $\boldsymbol{p}_u$ when user 2 at boresight ($\phi_2 = 0°$).

(b) Symbol error rate vs. signal-to-noise ratio when user 2 at boresight ($\phi_2 = 0°$).

(c) Symbol error rate vs. angle ϕ_2 of user 2 for $E_{\mathsf{s,tx}}/N_0 \,\hat{=}\, 15\,\text{dB}$.

Fig. 8. Sub-array analog beamforming architecture: Power-space profile and symbol error rate performance. Colors correspond to users: user 1 (—/-·-), user 2 (—/-·-), user 3 (—/-·-). Gray plots (—/-·-) represent results for conventional system without beamspace techniques for each user.

noncoherent detection fails since the users cannot be separated at the base station due to uniform power profiles. However, when the lens is present, noncoherent detection is enabled in the first place, whereas a small loss in performance is observed for coherent detection. An SNR gain can be noticed for user 2 compared to the users 1 or 3, which occurs due to the higher total receive power when located at boresight. The diversity order of the present scenario is three, which is equal to the number of different propagation paths. However, in case of the lens-embedded system, the diversity order is not fully reached, in particular for user 1 and 3. Here, the channel coefficients of the named users are less correlated in comparison to user 2 since the respective receive power is spread among a larger number of receive antennas (broadened PSP), but the SNR per antenna element is reduced leading to the corresponding losses in performance.

The symbol error rate performance as function of the angle ϕ_2 of user 2 at $E_{\mathsf{s,tx}}/N_0 \,\hat{=}\, 15\,\text{dB}$ is shown in Fig. 5c. It can be noted that when user 2 approaches one of the other users, the performance deteriorates for both users using noncoherent detection. This results from the overlapping of the respective power-space profiles. In case of BLAST, the SER of user 1 and 3 is not affected by the position of user 2. However, the SER of each individual user depends on the the actual position. Regarding the performance of user 2, the SER gets worse for larger $|\phi_2|$ due to the reduced receive power. Furthermore, a minor performance degradation of the second user can be seen around boresight with and without the lens system because of higher correlation present between the channel coefficients.

Next, the performance of the full-array architecture employing an analog beamforming network is analyzed. Since the number of beam ports N_b is kept the same as the number of receive antennas N_rx, 128 beams can be formed by the network in any arbitrary direction. The beams are evenly distributed in the defined scanning angle range of $\pm 45°$ resulting in approximately $0.7°$ resolution. Generally, when using an analog beamformer, comparable results are obtained as for the lens-embedded system (see Fig. 6). Here, the peak power of user 2 is slightly reduced when positioned at boresight (see Fig. 6a). This in turn worsens the SER performance slightly (see Fig. 6b and 6c). The minimal reduction in peak power originates from the lack of the associated angle bin at boresight of the beamformer. However, since the incoming waves impinge with a spatial spread, a characteristic peak can still be observed. User 1 and 3 perform worse than user 2, which is again due to the aperture loss. Furthermore, the diversity of the channel is not fully exploited for user 1 and 3 as already observed for the lens system.

B. Sub-Array Architecture

In the following, the sub-array architecture is examined offering the opportunity to relax the implementation requirements when the full-array lens or beamformer are not feasible. For this purpose, the given receive antenna array of $N_{\mathsf{rx}} = 128$ antennas is divided into $N_{\mathsf{sub}} = 8$ equal-size sub-arrays consisting of $N_{\mathsf{rx,sub}} = 16$ antennas.

Analyzing the sub-array lens architecture first, the previous full-array aperture D is downsized accordingly to $D' = 8\lambda$. The focal length is adapted to $f' = 5.2\lambda$ such that $f'/D' = 0.65$ to provide the same previously defined scanning angle range. Each sub-array is then equipped with a smaller sized lens version, respectively. Since all sub-array elements process the incoming signals individually and independently, the power-space profile exhibits a periodic pattern of the profile of a single sub-array as depicted in Fig. 7a. The distance between the individual user profiles diminishes due to the reduced aperture size of the lens. Regarding the symbol error rate performance, substantial gains can be observed for all users (in particular for user 1 and 3) in the coherent and, more importantly, in the noncoherent case (see Fig. 7b and 7c). The entire receiving array is illuminated more evenly, but still a characteristic power-profile is provided to separate the users. The individual user profiles exhibit no considerable differences in shape anymore (narrowed PSP) and the channel correlation is reduced as the total power is redistributed among small antenna groups. This in turn leads to an almost full exploitation of the channel diversity for all users (as it is the case for coherent reception without beamspace techniques). Note that user 2 still performs better due to the higher total receive power when located at boresight (SNR gain). However, the amount of degradation in performance is higher in the given case when user 2 approaches one of the other user. This is the result of the closely spaced individual user profiles starting to overlap as soon as the second user leaves the boresight direction. As a consequence, the user separability is reduced when applying the sub-array approach. The same applies to the sensitivity of the system. While employing the full-array system, the peak power of the user varies by 1.42 ($\approx 128/90°$) BS antenna positions per user angle ϕ_u, in case of the sub-array approach with $N_{\mathsf{sub}} = 8$ and $N_{\mathsf{rx,sub}} = 16$, the change amounts to 0.18 ($\approx 16/90°$) BS antenna positions per user angle ϕ_u.

Next, the sub-array approach is applied and evaluated for the analog beamforming structure. Here, the signals of the $N_{\mathsf{rx}} = 128$ antennas are processed by $N_{\mathsf{sub}} = 8$ equally constructed beamforming networks, where each has $N_{\mathsf{rx,sub}} = N_{\mathsf{b,sub}} = 16$ input and output (beam) ports, respectively. To maintain the prescribed scanning range, the corresponding beam angles are again evenly distributed in the range of $\pm 45°$. The results are illustrated in Fig. 8. Basically, the sub-beamformer performs almost equally to the sub-lens architecture. Again, a periodic pattern in the power-space profile can be seen. However, since the number of available angle bins is shrinked to 16, the angle resolution is reduced to roughly $5.6°$. Furthermore, the symbol error rate performance is enhanced compared to the full-array architecture, but the performance level of the sub-lens architecture is not fully achieved. This approach faces also the same user separability and sensitivity issues as described above.

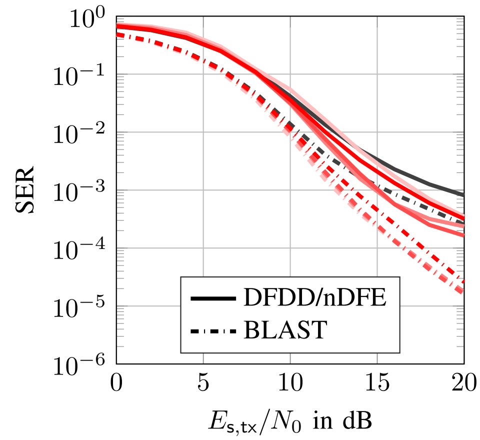

(a) Lens.

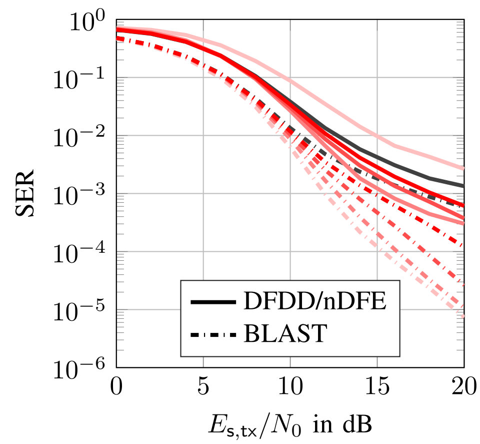

(b) Analog beamformer.

Fig. 9. Symbol error rate performance of user 1 when user 2 at boresight ($\phi_2 = 0°$) for full-array system (—/-·-) and for different number of sub-arrays ($N_{\mathsf{sub}} = 4$ (—/-·-), $N_{\mathsf{sub}} = 8$ (—/-·-), $N_{\mathsf{sub}} = 16$ (—/-·-), $N_{\mathsf{sub}} = 32$ (—/-·-)).

Fig. 9 illustrates the symbol error rate performance of the edge-positioned user 1 as function of the signal-to-noise ratio for the full-array system and for different number of sub-arrays N_{sub} utilizing the analog beamformer or the dielectric lens approach, respectively. It is assumed that user 2 is located at boresight. As previously stated, the sub-array approach is superior compared to the full-array system. Regarding noncoherent detection, a degradation in performance can be observed when the number of sub-arrays is very large. This is due to the fact that as N_{sub} is increased, the induced power of the users are spread over a larger number of antennas per sub-array resulting in an overlap of the individual PSPs, i.e., the users cannot be separated anymore when N_{sub} is too large. Here, the

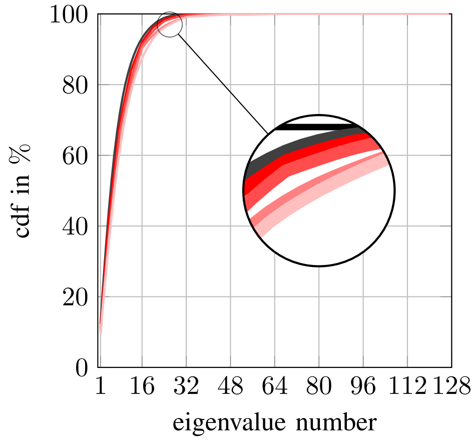

(a) Lens.

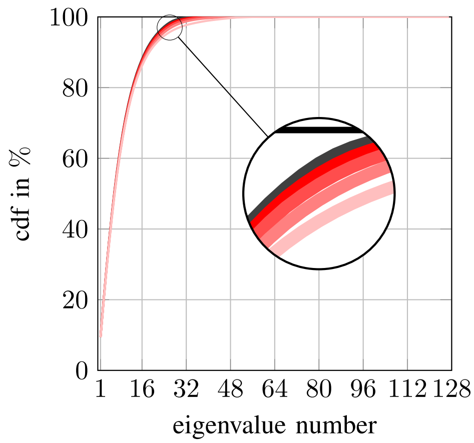

(b) Analog beamformer.

Fig. 10. Cumulative distribution function (cdf) of the eigenvalues $\boldsymbol{\Lambda}_u$ of the covariance matrix $\boldsymbol{Q}_u = \mathrm{E}\{\boldsymbol{h}_u\boldsymbol{h}_u^{\mathsf{H}}\} = \boldsymbol{V}_u\boldsymbol{\Lambda}_u\boldsymbol{V}_u^{-1}$ of user 1 for a full-array system (—) and for a different number of sub-arrays ($N_{\mathsf{sub}} = 4$ (—), $N_{\mathsf{sub}} = 8$ (—), $N_{\mathsf{sub}} = 16$ (—), $N_{\mathsf{sub}} = 32$ (—)).

analog beamformer shows greater susceptibility because of the mentioned angular bin issue. Best performance is achieved for $N_{\mathsf{sub}} = 8$ or $N_{\mathsf{sub}} = 16$. On the contrary, the symbol error rate performance of the coherent detection improves and a slight increase in diversity order (approaching the maximal channel diversity) can be observed for larger N_{sub}, in particular for the analog beamformer. Analyzing the cumulative distribution function (cdf) of the eigenvalues $\boldsymbol{\Lambda}_u$ of the covariance matrix $\boldsymbol{Q}_u = \mathrm{E}\{\boldsymbol{h}_u\boldsymbol{h}_u^{\mathsf{H}}\} = \boldsymbol{V}_u\boldsymbol{\Lambda}_u\boldsymbol{V}_u^{-1}$ of user 1, where $\boldsymbol{V}_u$ contains the eigenvectors of $\boldsymbol{Q}_u$ along its columns and $\boldsymbol{\Lambda}_u$ contains the corresponding eigenvalues along the diagonal in decreasing order, reveals a reduction of the overall channel correlations (see Fig. 10). The depicted cdf represents the amount of information contained in the eigenvectors for a given eigenvalue number. There is no correlation present when all eigenvalues are identical (cdf is a straight line). If there exist a few strong eigenvalues, which contain most of the power, the channel vector is likely to be spanned by the respective eigenvectors. This is accompanied by strong correlation [39]. For the full-array beamformer and full-array lens system, the first 26 largest eigenvalues contain 99% of the power leading to a correlated channel. Applying the sub-array approach, the cdf is more flattened for an increasing number of sub-arrays N_{sub} in both systems, i.e., the power is spread over a larger number of eigenvalues corresponding to a reduction in correlation. For comparison, in case of the analog beamformer using $N_{\mathsf{sub}} = 32$ sub-arrays, the first 42 largest eigenvalues contain 99% of the power.

V. Conclusion

In this paper, a noncoherent massive MIMO uplink system employing beamspace techniques has been assessed. First, the corresponding beamspace models, i.e., a dielectric lens and an analog beamformer network were derived and integrated in a cluster-based channel model. Then, it was successfully demonstrated that by means of a lens or a beamforming structure, a characteristic PSP can be provided at the BS. This in turn enables noncoherent detection even in scenarios, where the users are in the far-field, or rather, plane-waves arrive at the BS.

Analyzing the symbol error rate performance revealed that the lens-embedded system and the analog beamforming structure perform almost identically. The noncoherent detection scheme is dependent on the actual user location. Performance degrades when the user moves away from boresight of the array or when users are located very close. A significant performance enhancement is obtained when the sub-array system is employed instead of the full-array system. This provides a periodic PSP and a more even illumination of the entire receiving array at the same time. The maximal channel diversity is almost reached for all users, which is not the case for the full-array system. However, a slight difference in performance can be noticed between lens and analog beamforming network, which is due to the reduced angular resolution of the beamformer.

The performance was evaluated for a three-user scenario in order to analyze the principal behavior of beamspace techniques in conjunction with noncoherent detection. The users are assumed to be static and the channel is constant during each transmission burst. When users are in mobility, the PSP varies accordingly at the BS. No impact on the performance is expected, while the individual user profiles show almost no overlap and the transmission is within the coherence time. Additionally, more users can be accommodated as long as the individual PSPs do not dramatically overlap. This holds for full-array and sub-array architecture, whereby the latter can serve less users due to the reduced user separability. A better separation of the users is obtained around boresight, since the power footprint is narrow. Noteworthy, the spatial spread at the BS impacts the power footprint width as well. As a consequence, more users can be served when the spatial spread is less. Compared to coherent detection, the total number of optimally supported users can be smaller [40]. However, the complexity of the system is reduced since no accurate channel state information and no pilot symbol allocation is required. The associated channel estimation errors and spectral efficiency losses have a severe impact on the system performance [13], which have not been taken into account in this paper. Moreover, utilizing the power-space profile instead of the actual channel estimates as in our proposed detection scheme may also be advantageous in dynamic scenarios. Since the power-space profile is only angle-dependent, the profiles are robust especially to radial user movements towards or away from the base station. On the contrary, outdated channel state information due to users in mobility can be very harmful when CSI-based detection is applied [41], [42].

In summary, despite the reduced user separability, the sub-array architecture is a very promising approach when non-coherent detection schemes are applied at the BS. Moreover, this approach offers the opportunity to relax the design requirements for a practical implementation. As future work, the optimization of the number of sub-arrays and the corresponding number of receive antennas per sub-array remains, since they affect the induced power distribution at the receiver and thus, the user separability and the number of users, which can be accommodated. Furthermore, there are additional degrees of freedom when specifying the scanning angle range of each sub-array. For instance, applying the analog beamforming approach, the scanning angle range can be sectorized and each sub-array processes the signals from an assigned sector.

Acknowledgment

This work was funded by the Deutsche Forschungsgemeinschaft (DFG, German Research Foundation) — WA 3506/5-1 and FI 982/12-1.

References

[1] A. Gupta and R. K. Jha, "A Survey of 5G Network: Architecture and Emerging Technologies," *IEEE Access*, vol. 3, pp. 1206–1232, 2015.

[2] F. Rusek, D. Persson, B. K. Lau, E. G. Larsson, T. L. Marzetta, O. Edfors, and F. Tufvesson, "Scaling Up MIMO: Opportunities and Challenges with Very Large Arrays," *IEEE Signal Processing Magazine*, vol. 30, no. 1, pp. 40–60, Jan. 2013.

[3] E. G. Larsson, O. Edfors, F. Tufvesson, and T. L. Marzetta, "Massive MIMO for Next Generation Wireless Systems," *IEEE Communications Magazine*, vol. 52, no. 2, pp. 186–195, Feb. 2014.

[4] S. Yang and L. Hanzo, "Fifty Years of MIMO Detection: The Road to Large-Scale MIMOs," *IEEE Communications Surveys & Tutorials*, vol. 17, no. 4, pp. 1941–1988, 2015.

[5] T. L. Marzetta, "Noncooperative Cellular Wireless with Unlimited Numbers of Base Station Antennas," *IEEE Transactions on Wireless Communications*, vol. 9, no. 11, pp. 3590–3600, Nov. 2010.

[6] J. Guey and L. Larsson, "Modeling and Evaluation of MIMO Systems Exploiting Channel Reciprocity in TDD Mode," in *IEEE Vehicular Technology Conference (VTC)*, Sep. 2004.

[7] M. Rui, C. Ruo, W. Chaowei, and W. Weidong, "Downlink Transmission Scheme for Massive MU-MIMO System with Reduced CSI," in *IEEE International Conference on Network Infrastructure and Digital Content*, Sep. 2014.

[8] M. S. Sim, J. Park, C. Chae, and R. W. Heath, "Compressed Channel Feedback for Correlated Massive MIMO Systems," *Journal of Communications and Networks*, vol. 18, no. 1, pp. 95–104, Feb. 2016.

[9] O. Elijah, C. Y. Leow, T. A. Rahman, S. Nunoo, and S. Z. Iliya, "A Comprehensive Survey of Pilot Contamination in Massive MIMO—5G System," *IEEE Communications Surveys & Tutorials*, vol. 18, no. 2, pp. 905–923, 2016.

[10] J. Jose, A. Ashikhmin, T. L. Marzetta, and S. Vishwanath, "Pilot Contamination and Precoding in Multi-Cell TDD Systems," *IEEE Transactions on Wireless Communications*, vol. 10, no. 8, pp. 2640–2651, Aug. 2011.

[11] A. Schenk and R. F.H. Fischer, "Noncoherent Detection in Massive MIMO Systems," in *17th International ITG Workshop on Smart Antennas (WSA)*, Mar. 2013, pp. 1–8.

[12] R. F.H. Fischer and M. Bense, "Noncoherent Decision-Feedback Equalization in Massive MIMO Systems," in *International Zurich Seminar on Communications (IZS)*, Feb. 2014, pp. 112–115.

[13] R. F.H. Fischer, M. Bense, and C. Stierstorfer, "Noncoherent Joint Decision-Feedback Detection in Multi-User Massive MIMO Systems," in *18th International ITG Workshop on Smart Antennas (WSA)*, March 2014, pp. 1–8.

[14] S. Bucher, G. Yammine, R. F.H. Fischer, and C. Waldschmidt, "Influence of Channel Parameters on Noncoherent Massive MIMO Systems," in *22nd International ITG Workshop on Smart Antennas (WSA)*, Mar. 2018.

[15] S. Bucher, A. N. Ragab, G. Yammine, R. F.H. Fischer, and C. Waldschmidt, "Antenna Design For Noncoherent Massive MIMO Systems," in *15th International Symposium on Wireless Communication Systems (ISWCS)*, Aug. 2018.

[16] R. Rotman, M. Tur, and L. Yaron, "True Time Delay in Phased Arrays," *Proceedings of the IEEE*, vol. 104, no. 3, pp. 504–518, Mar. 2016.

[17] A. Grau, J. Romeu, S. Blanch, L. Jofre, and F. D. Flaviis, "Optimization of Linear Multielement Antennas for Selection Combining by Means of a Butler Matrix in Different MIMO Environments," *IEEE Transactions on Antennas and Propagation*, vol. 54, no. 11, pp. 3251–3264, Nov. 2006.

[18] H. Krim and M. Viberg, "Two Decades of Array Signal Processing Research: The Parametric Approach," *IEEE Signal Processing Magazine*, vol. 13, no. 4, pp. 67–94, Jul. 1996.

[19] B. V. Veen and K. Buckley, "Beamforming: A Versatile Approach to Spatial Filtering," *IEEE ASSP Magazine*, vol. 5, no. 2, pp. 4–24, Apr. 1988.

[20] D. G. Manolakis, V. K. Ingle, and S. M. Kogon, Eds., *Statistical and Adaptive Signal Processing: Spectral Estimation, Signal Modeling, Adaptive Filtering and Array Processing*. Artech House, 2005.

[21] Y. Zeng, L. Yang, and R. Zhang, "Multi-User Millimeter Wave MIMO With Full-Dimensional Lens Antenna Array," *IEEE Transactions on Wireless Communications*, vol. 17, no. 4, pp. 2800–2814, Apr. 2018.

[22] Y. Zeng and R. Zhang, "Millimeter Wave MIMO With Lens Antenna Array: A New Path Division Multiplexing Paradigm," *IEEE Transactions on Communications*, vol. 64, no. 4, pp. 1557–1571, Apr. 2016.

[23] Y. Zeng, R. Zhang, and Z. N. Chen, "Electromagnetic Lens-Focusing Antenna Enabled Massive MIMO: Performance Improvement and Cost Reduction," *IEEE Journal on Selected Areas in Communications*, vol. 32, no. 6, pp. 1194–1206, Jun. 2014.

[24] Y. Zeng and R. Zhang, "Cost-Effective Millimeter-Wave Communications with Lens Antenna Array," *IEEE Wireless Communications*, vol. 24, no. 4, pp. 81–87, Aug. 2017.

[25] T. Kwon, Y. Lim, and C. Chae, "Limited Channel Feedback for RF Lens Antenna Based Massive MIMO Systems," in *International Conference on Computing, Networking and Communications (ICNC)*, Feb. 2015, pp. 6–10.

[26] T. Kwon, Y. G. Lim, B. W. Min, and C. B. Chae, "RF Lens-Embedded Massive MIMO Systems: Fabrication Issues and Codebook Design," *IEEE Transactions on Microwave Theory and Techniques*, vol. 64, no. 7, pp. 2256–2271, Jul. 2016.

[27] G. Yammine, S. Bucher, and R. F.H. Fischer, "Noncoherent Detection for an EM-Lens-Enabled Massive MIMO System," in *International ITG Conference on Systems, Communication and Coding (SCC)*, Feb. 2019.

[28] B. Cetinoneri, Y. A. Atesal, and G. M. Rebeiz, "An 8×8 Butler Matrix in 0.13-µm CMOS for 5–6-GHz Multibeam Applications," *IEEE Transactions on Microwave Theory and Techniques*, vol. 59, no. 2, pp. 295–301, Feb. 2011.

[29] W. Rotman and R. Turner, "Wide-Angle Microwave Lens for Line Source Applications," *IEEE Transactions on Antennas and Propagation*, vol. 11, no. 6, pp. 623–632, Nov. 1963.

[30] Y. Gao, M. Khaliel, F. Zheng, and T. Kaiser, "Rotman Lens Based Hybrid Analog–Digital Beamforming in Massive MIMO Systems: Array Architectures, Beam Selection Algorithms and Experiments," *IEEE Transactions on Vehicular Technology*, vol. 66, no. 10, pp. 9134–9148, Oct. 2017.

[31] J. W. Goodman, *Introduction to Fourier Optics*. McGraw-Hill, 1996.

[32] M. Jiang, Z. N. Chen, Y. Zhang, W. Hong, and X. Xuan, "Metamaterial-Based Thin Planar Lens Antenna for Spatial Beamforming and Multibeam Massive MIMO," *IEEE Transactions on Antennas and Propagation*, vol. 65, no. 2, pp. 464–472, Feb. 2017.

[33] M. A. Al-Joumayly and N. Behdad, "Wideband Planar Microwave Lenses Using Sub-Wavelength Spatial Phase Shifters," *IEEE Transactions on Antennas and Propagation*, vol. 59, no. 12, pp. 4542–4552, Dec. 2011.

[34] L. Liu, C. Oestges, J. Poutanen, K. Haneda, P. Vainikainen, F. Quitin, F. Tufvesson, and P. D. Doncker, "The COST 2100 MIMO Channel Model," *IEEE Wireless Communications*, vol. 19, no. 6, pp. 92–99, Dec. 2012.

[35] R. Verdone and A. Zanella, Eds., *Pervasive Mobile and Ambient Wireless Communications*. Springer London, 2012.

[36] G. Yammine, R. F.H. Fischer, and C. Waldschmidt, "On the Influence of the Antenna Pattern in Noncoherent Massive MIMO Systems," in *International Symposium on Wireless Communication Systems (ISWCS)*, Aug. 2015, pp. 391–395.

[37] G. J. Foschini, D. Chizhik, M. J. Gans, C. Papadias, and R. A. Valenzuela, "Analysis and Performance of Some Basic Space-Time Architectures," *IEEE Journal on Selected Areas in Communications*, vol. 21, no. 3, pp. 303–320, Apr. 2003.

[38] K. Pedersen, P. Mogensen, and B. Fleury, "Power Azimuth Spectrum in Outdoor Environments," *Electronics Letters*, vol. 33, no. 18, p. 1583, 1997.

[39] E. Björnson, J. Hoydis, and L. Sanguinetti, "Massive MIMO Networks: Spectral, Energy, and Hardware Efficiency," *Foundations and Trends® in Signal Processing*, vol. 11, no. 3-4, pp. 154–655, 2017.

[40] E. Björnson, E. G. Larsson, and M. Debbah, "Massive MIMO for Maximal Spectral Efficiency: How Many Users and Pilots Should Be Allocated?" *IEEE Transactions on Wireless Communications*, vol. 15, no. 2, pp. 1293–1308, Feb. 2016.

[41] M. Stojanovic, J. Proakis, and J. Catipovic, "Analysis of the Impact of Channel Estimation Errors on the Performance of a Decision-Feedback Equalizer in Fading Multipath Channels," *IEEE Transactions on Communications*, vol. 43, no. 2, pp. 877–886, Feb. 1995.

[42] W. Peng, F. Adachi, S. Ma, J. Wang, and T.-S. Ng, "Effects of Channel Estimation Errors on V-BLAST Detection," in *IEEE Global Telecommunications Conference (GLOBECOM)*, Dec. 2008.

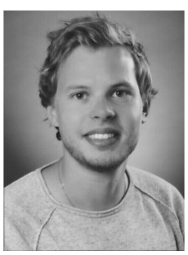

Stephan Bucher (GS'16) received the M.Sc. degree in electrical engineering (with a focus on communication technology) from the University of Ulm, Ulm, Germany, in 2016. He is currently pursuing the Ph.D. degree in electrical engineering at the Institute of Microwave Engineering, Ulm University. His current research interests include noncoherent multi-user detection techniques, and massive multiple-input/multiple-output (MIMO) systems.

George Yammine (GS'19) was born in Zakrit, Lebanon, in 1986. He received the B.E. degree in computer and communications engineering from Notre Dame University, Louaize, Lebanon, in 2010, and the M.Sc. degree in communications technology from Ulm University, Ulm, Germany, in 2014, for which he was awarded the ARGUS Science Award 2014, from Airbus Defence and Space. He joined the Institute of Communications at Ulm University in 2015, working toward the Ph.D. degree. His research interests include noncoherent detection techniques, and massive multiple-input/multiple-output (MIMO) systems.

Robert F.H. Fischer (S'93–A'96–M'99–SM'10) received the Dr.-Ing. and Habilitation degrees from the University of Erlangen–Nürnberg, Erlangen, Germany, in 1996 and 2001, respectively. From 1992 to 1996, he was a Research Assistant with the Telecommunications Institute, University of Erlangen–Nürnberg. In 1997, he was with the IBM Research Laboratory, Zürich, Switzerland. In 1998, he returned to the University of Erlangen–Nürnberg, and in 2005, he spent a sabbatical with ETH Zürich, Zürich. Since 2011, he has been a Full Professor with the University of Ulm, Ulm, Germany. He is currently teaching the undergraduate and graduate courses on signals and systems and digital communications. He authored the textbook Precoding and Signal Shaping for Digital Transmission (Wiley, 2002). His current research interests include fast, reliable, and secure digital transmission including single-carrier and multicarrier modulation techniques, information theory, coded modulation, digital communications, signal processing, and especially precoding and shaping techniques. Dr. Fischer was a recipient of the Dissertation Award from the Technische Fakultät, University of Erlangen–Nürnberg, in 1997, the Publication Award of the German Society of Information Techniques in 2000, the Wolfgang Finkelnburg Habilitation Award in 2002, and the Philipp–Reis–Preis in 2005.

Christian Waldschmidt (S'01–M'05–SM'13) received the Dipl.-Ing. (M.S.E.E.) and the Dr.-Ing. (Ph.D.E.E.) degrees from the University Karlsruhe (TH), Karlsruhe, Germany, in 2001 and 2004, respectively. From 2001 to 2004 he was a Research Assistant at the Institut für Höchstfrequenztechnik and Elektronik (IHE), Universität Karlsruhe (TH), Germany. Since 2004 he has been with Robert Bosch GmbH, in the business units Corporate Research and Chassis Systems. He was heading different research and development teams in microwave engineering, rf-sensing, and automotive radar.

In 2013 Christian Waldschmidt returned to academia. He was appointed as the Director of the Institute of Microwave Engineering at University Ulm, Germany, as full professor. The research topics focus on radar and rf-sensing, mm-wave and submillimeter-wave engineering, antennas and antenna arrays, rf and array signal processing. He authored or coauthored over 150 scientific publications and more than 20 patents. Additionally, he is chair of IEEE MTT-27 Technical Committee (wireless enabled automotive and vehicular applications), executive committee board member of the German MTT/AP joint chapter, and member of the ITG committee Microwave Engineering (VDE). In 2015 and 2017 he served as the TPC chair and in 2018 as Chair of the IEEE MTT International Conference on Microwaves for Intelligent Mobility. Since 2018, Christian Waldschmidt serves as associate editor for IEEE MTT Microwave Wireless Components Letters (MWCL). He is a reviewer for multiple IEEE transactions and several conferences like IMS and EUMW.